

# Mode Transition of a Flexible Film Motion in the Circular Cylinder Wake

Fan Duan<sup>1</sup>, Jin-Jun Wang<sup>1,\*</sup>

<sup>1</sup>: Fluid Mechanics Key Laboratory of Education Ministry, Beihang University, Beijing, 100191, PR China

\*Corresponding author: [jjwang@buaa.edu.cn](mailto:jjwang@buaa.edu.cn)

**Keywords:** Fluid-structure interactions, Vortex dynamics, Continuous wavelet transform, Virtual dye visualization.

## ABSTRACT

The fluid-structure interaction between a flexible film and the wake of a circular cylinder is an abstract of a series of natural phenomena like flag flapping and fish swimming. Diverse patterns of both solid deformation and fluid dynamics arise in this coupling system as the nondimensional parameters are varied. In our recent experiments, we find that beyond the extensively studied periodic coupling process, irregular processes also emerge in this system under specific conditions. However, due to the complexity inherent in the irregular coupling processes, no in-depth investigation into this topic is available yet. In this work, we delve into the irregular aperiodic flutter of a flexible film behind a circular cylinder in the uniform flow as well as the related irregular evolution of flow structures. Two representative cases of film streamwise length ( $L/D$ ) pertinent to the irregular process, specifically  $L/D = 3.0$  and  $L/D = 4.0$ , have been investigated experimentally in the wind tunnel with time-resolved synchronized measurements of film deformation and flow field. Continuous wavelet transform and virtual dye visualization are employed to extract the time-frequency characteristics of film motion and Lagrangian coherent structures in the flow fields during the film's irregular flutter, respectively. It is determined that the irregular flutter is aperiodic in terms of the overall view, but it also encompasses transient quasi-periodic stages as its motion modes alter. Hence, we term this irregular flutter as the "hybrid flutter" state. In the quasi-periodic stages of the hybrid flutter, the large-scale vortex structures are periodically formed on the surfaces of the film and evolve in the wake as a Kármán vortex street. The periodic formation of large-scale vortices exerts periodic alternating force on the film, which, therefore, leads to the quasi-periodic flutter of the film with the second-order mode. By comparison, the aperiodic stage entails the significant extension of the separated shear layers in such a way that the whole film is enveloped by the shear layers; then, large-scale vortices are formed downstream of the film's trailing edge. In this scenario, no periodic force is acted on the film; as a result, the film flutters aperiodically with the first-order mode.

---

## 1. Introduction

A flexible film/filament placed in the wake of a circular cylinder experiences unsteady forces due to the large-scale vortex shedding from the cylinder. It has responses to the unsteady force and,

therefore, exhibits vortex-induced flutter. This is an archetype of fluid-structure interactions (FSI), which can be deemed as the physical abstract of a series of natural phenomena, such as the sway of tentacles behind the umbrella-shaped body of a jellyfish (Miles & Battista, 2019), the undulatory propulsion of a larval zebrafish (T. Wang et al., 2021) and the Kármán gaiting of a trout in the periodic vortices (Liao, 2007). The mechanisms underlying these phenomena are of great importance in the investigation of biological locomotion and then conducive to bio-inspired engineering. The flapping flag hung on a flagpole is another representative phenomenon for such FSI (M. J. Shelley & Zhang, 2011). When the material of the flag is the thin flexible piezoelectric film, utilizing the flapping of the flag, it has been achieved to harvest energy from a wavy or windy environment, i.e., the deformation of the piezoelectric film converts the elastic strain energy to electricity (Taylor et al., 2001; Yu & Liu, 2015). Furthermore, in the field of flow control, a flexible film behind a circular cylinder has also been demonstrated to be an effective passive device for the reduction of drag (Sharma & Dutta, 2020; Shukla et al., 2023), vibration (Cui et al., 2022; Sahu et al., 2019), and noise (Duan & Wang, 2021) originating from the vortex shedding.

In numerical simulations at low Reynold numbers, for example,  $Re = 80 \sim 200$  (Lee & You, 2013; Pfister & Marquet, 2020; Furquan & Mittal, 2021), the FSI between the film and the cylinder wake is always a periodic process. The numerical simulation at  $Re = 150$  of Furquan & Mittal (2021) shows that with the alteration of the dimensionless parameters, the film motion transitions among several periodic states, and the contribution of different intrinsic modes of the film to the deformation changes as well. In the flow fields, several periodic vortex shedding patterns associated with different motion modes of the film are also observed from the simulation results, including 2S, 2P, P+S and 2P+2S modes. However, in the experimental investigations, the dynamics of the film are richer. The film also experiences aperiodic processes, which have been reported by Shukla et al. (2023) and Duan & Wang (2021, 2024). The results in the experiments of Shukla et al. (2023) indicate that with the transition of the film motion from the periodic mode to the aperiodic mode, the amplitude of the film undergoes a sudden decrease. For the film with a dimensionless length of  $L/D = 2.0$  ( $L$  is the streamwise length of the film and  $D$  is the cylinder diameter), its motion pattern even becomes no longer symmetric with respect to the wake centerline during the aperiodic state. In the research of Duan & Wang (2024), it is found that the aperiodic motion of the film tends to chaos with the largest Lyapunov exponent  $\lambda_1 > 0$  and a predictable time of only  $O(10^{-2})$  s. Moreover, the aperiodic motion is identified to have a superior performance in suppressing the Aeolian tone from the circular cylinder, where an 18 dB reduction is achieved as the streamwise length of the film is  $L/D = 1.0$  (Duan & Wang, 2021). In this situation, the spectrum of the film motion features a concentration of energy in the low-frequency broadband region, which is smaller than the dominant frequency of vortex shedding by an order of magnitude (Duan & Wang, 2021). In the realm of biological locomotion, the special behavior, termed “entraining state”, of a fish behind an obstacle in the river (Webb, 1998; Liao, 2007) bears a resemblance to the aperiodic motion of the film. In the entraining state, the fish’s head is close to the rear of the bluff body, and the

fish's body keeps pretty straight with an irregular small-amplitude flutter, which is believed to be energetically favorable (Taguchi & Liao, 2011). The existing research on the entraining state focuses mainly on the biological mechanisms, for instance, the metabolic expenditure of the fish. However, scarcely any in-depth analysis of the dynamic characteristics of the entraining state is available, which is merely documented as an indiscernible pattern in literature (Liao, 2007). Given the kinematic similarity between the aperiodic flutter of the film and the entraining state of the fish, the methods developed from the analyses of the film motion hold promise for the study on the dynamics of the fish's entraining state.

Compared with the periodic interaction between the film and the cylinder wake, the aperiodic interaction is bound to come with more nuanced and intricate evolution of the flow structures, due to its inherent irregularity. Hence, the investigation into the aperiodic interaction requires, on the one hand, the precise synchronized measurements of the flow field and film deformation, and on the other hand, sophisticated analysis methods to dig out the details in the FSI system. In our recent experiment (Duan & Wang, 2024), it is observed that at specific streamwise lengths, the film consistently adopts irregular aperiodic motion, where the first-order mode and the second-order mode are alternately featured in the film deformation. This is a spontaneous alternate process, which emerges even though the external conditions like freestream velocity and temperature remain unchanged. In this work, we attempt to explore the related mechanisms underlying the different modes of the aperiodic motion. The continuous wavelet transform and the virtual dye visualization are employed to perform quantitative analyses on the film motion and the flow structures, respectively.

## 2. Experimental set-up

The experiment was performed in the open-circuit low-speed wind tunnel D6 at Beihang University (Fig. 1a). The test section of the wind tunnel has a length of 5 m and a rectangular cross-section. The experimental model is comprised of a circular cylinder and a flexible film, which was vertically placed in the wind tunnel (Figs. 1a and 1b). The distance between the experimental model and the wind tunnel nozzle was 0.9 m, at which the rectangular cross-section of the test section was 430 mm  $\times$  500 mm (width  $\times$  height). The diameter of the cylinder  $D = 200$  mm (Fig. 1c), and the freestream velocity  $U_\infty = 10$  m s<sup>-1</sup> yielded a cylinder diameter-based Reynolds number of  $Re_D = 1.33 \times 10^4$  as the temperature of the test section was 21 °C. The spatial Cartesian coordinate system was defined in such a way that the  $x$ ,  $y$  and  $z$  axes aligned with the streamwise, vertical and spanwise directions, respectively, and the origin was set at the center of the mid-span cross-section of the cylinder model (Fig. 1). The transparent Polyethylene Terephthalate (PET) membrane was selected to fabricate the flexible films in the experiment. The thickness, density, Young's modulus and the spanwise height of the fabricated films were  $h = 0.10$  mm,  $\rho_s = 1.32 \times 10^3$  kg m<sup>-3</sup>,  $E = 2.1 \times 10^3$  MPa and  $b = 0.24$  m, respectively, which yield a bending stiffness  $B = Ebh^3/12 = 4.2 \times 10^{-5}$  N m<sup>2</sup>. The

film was attached to the cylinder rear with the clamped condition; for details of the connection between the film and the cylinder, one can refer to our previous research (Duan & Wang, 2024). Here, the spanwise height of the film  $b = 0.24$  m was smaller than that of the cylinder,  $b = 0.5$  m, so that the film only covered the middle portion of the cylinder, from  $z/D = -6$  to  $z/D = 6$  (see Fig. 1b). Under this condition, the influences of the end flow of the cylinder model on the film motion was avoided. The streamwise length of the film was changed from  $L/D = 0.5$  to  $L/D = 6$ —more precisely,  $L/D = 0.5, 1, 1.5, 2, 2.5, 3, 4, 5$  &  $6$ , respectively (Fig. 1c). Then, the two critical non-dimensional parameters, the effective bending stiffness  $K_B$  and the mass ratio  $S$  that govern the FSI system were  $K_B = 1.46 \sim 8.82 \times 10^{-4}$  and  $S = 10.98 \sim 0.91$ , respectively. Here,  $K_B$  is defined as  $K_B = B / (\rho_f U_\infty^2 b L^3)$ , while  $S$  is  $S = \rho_s h / (\rho_f L)$  (Duan & Wang, 2024; M. Shelley et al., 2005), where  $\rho_f$  is the density of the oncoming flow.

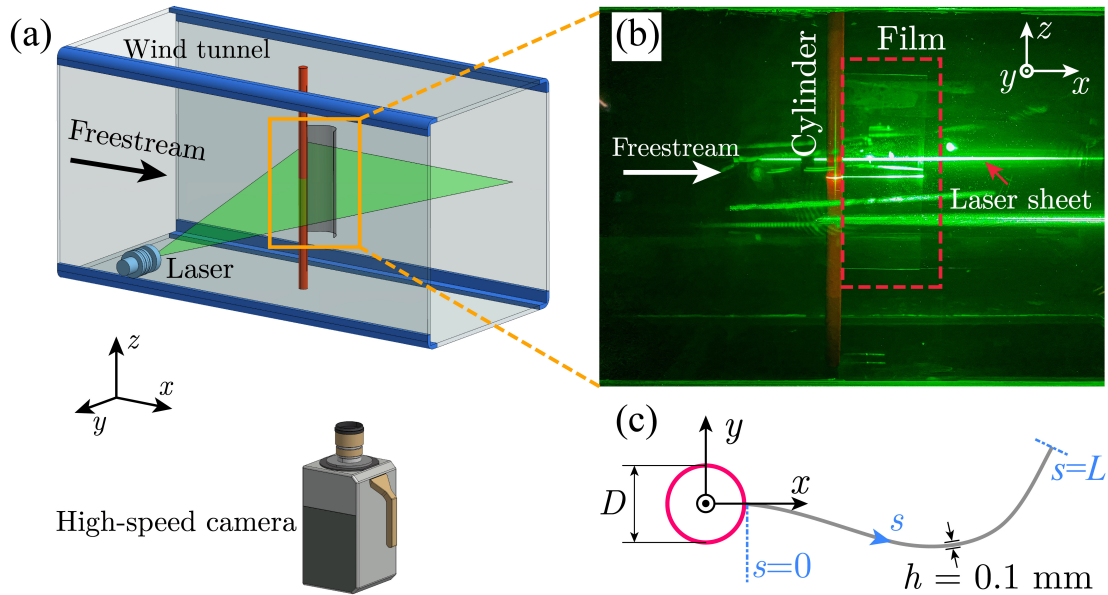


**Figure 1.** Details of experiments. (a) Sketch of the experimental system. (b) Photograph of experimental model. (c) Cross-section of the experimental model. Here, the Lagrangian curvilinear coordinate  $s$  is defined along the film length, where  $s = 0$  and  $s = L$  correspond to the fixed leading edge and the free trailing edge, respectively.

The flow fields and the film's instantaneous deformations were measured together by a two-dimensional time-resolved particle image velocimetry (PIV) system. The tracer particles for PIV and the transparent film were illuminated by a high-repetition-rate double-pulsed Nd:YLF laser with a frequency of 800 Hz, whose beam was expanded to a thin sheet. The laser sheet coincided precisely with the mid-span plane at  $z = 0$ . A high-speed CMOS camera (PCO dimax HS4) with a resolution adjusted to  $1500 \times 2000$  pixels was arranged right below the wind tunnel to capture grayscale image pairs, which embodied the information of both the tracer particles and film deformations. With a Nikon 50 mm F/1.8D lens mounted on the camera, the physical field of view was about  $0 < x < 12D$  and  $-4D < y < 4D$ . The total sampling time was larger than 20 s, corresponding to more than  $1.6 \times 10^4$  pairs of images. The velocity fields were obtained by processing

the image pairs with the multipass iterative Lucas–Kanade algorithm (Champagnat et al., 2011). Then, the tracer particles were filtered out from the grayscale images, and the instantaneous deformation curves of the film were extracted from the filtered images using digital image processing techniques (Gonzalez & Woods, 2017).

### 3. Results

With the film length changed from  $L/D = 0.5$  to  $L/D = 6.0$  incrementally, we observe four representative motion states of the film (Fig. 2). They are stable state for  $L/D \lesssim 0.5$  (Fig. 2a), single-mode flutter state for  $L/D = 1.0 \sim 2.0$  (Fig. 2b), hybrid flutter state for  $L/D = 2.5 \sim 4.0$  (Figs. 2c and 2d) and periodic flapping state for  $L/D \gtrsim 5.0$  (Fig. 2e), respectively. Here, the “single-mode flutter” signifies the film deforming always with its first-order mode, while the “hybrid flutter” means the film alternately exhibits deformation that either only follows the first-order mode or incorporates an evident feature of the second-order mode. For the sake of convenience, we adopt the term “deflection” to denote the transient deformation dominated by the first-order mode while the term “flection” denotes the transient deformation with an evident feature of the second-order mode. The film motion shows nearly flawless periodicity during the flapping state ( $L/D \gtrsim 5.0$ ), where the flow fields and the film undergo a mutual locked-in interaction, which has been comprehensively analysed in our previous investigation; for details, one can refer to Duan & Wang (2024). As for the single-mode flutter state ( $L/D = 1.0 \sim 2.0$ ), the film motion assumes a pseudo-periodic nature, which possesses an approximately consistent dominant frequency but an irregularly varying amplitude. In contrast, the “hybrid flutter” appears completely aperiodic and shows some random characteristics (Figs. 2c and 2d) due to the spontaneous mode alternation. This is an intriguing phenomenon but is usually overlooked. The fluid-structure interaction mechanisms underlying the hybrid flutter are indefinite as yet. We will discuss two intriguing problems about the hybrid flutter hereinafter. One is the dynamics of how the film interacts with the cylinder wake in the hybrid state, while the other is what happens as the mode changes from the deflection to the flection.

To intuitively show the irregularity of the hybrid flutter, we present the time histories of trailing edges for the films with  $L/D = 3.0$  and  $L/D = 4.0$  in Figs. 3(a) and 4(a), respectively. Both of the two time histories are disordered since on the one hand, no dominant frequency can be directly discerned, while on the other hand, the instantaneous amplitude undergoes irregular changes. Considering the irregularity of the trailing-edge motion, we utilize the continuous wavelet transform (CWT) to extract the time-frequency information embodied in the time traces. Compared to the discrete Fourier transform or its equivalent, the fast Fourier transform, CWT stands out by not only resolving the frequency components in the signal, but also pinpointing the times at which specific frequencies occur (J.-S. Wang & Wang, 2021). Furthermore, CWT provides high temporal resolution for the high-frequency components while high resolution of frequency for the

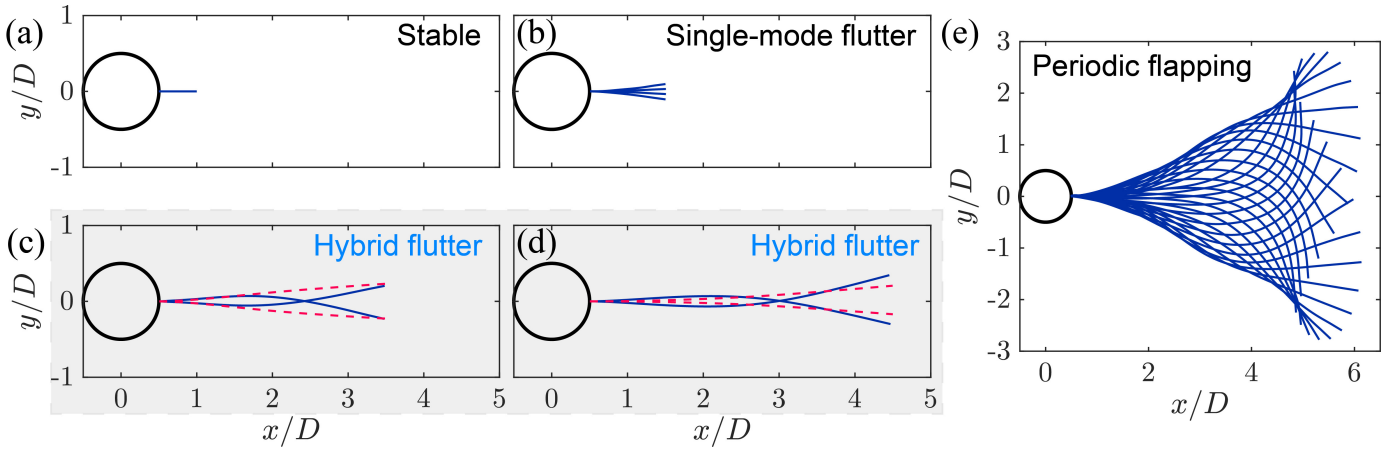


**Figure 2.** Motion states of the film. (a-e) For  $L/D = 0.5$ ,  $L/D = 1.0$ ,  $L/D = 3.0$ ,  $L/D = 4.0$  and  $L/D = 6.0$ , respectively. In panels (c) and (d), both the films undergo hybrid flutter, which is characterized by the spontaneous alternation between the deflection mode (the first-order mode; see the dashed red deformation curves) and flection mode (the second-order mode; see the solid blue deformation curves).

low-frequency components, thus emerging as a potent analytical technique for irregular data with transient events (Mallat, 1999). Figures 3(b) and 4(b) show the CWT results for the temporal traces of the trailing edge in Figs. 3(a) and 4(a), respectively. Here, the analytic morse wavelet is selected to perform the CWT, and  $L_1$  normalization is implemented to the wavelet; in this way, the magnitude of the time-frequency spectrum is equal to the amplitude of oscillatory components in the inputted data across different scales. The most prominent feature in both spectra is the occurrence of the high-magnitude region. For  $L/D = 3.0$ , a dominant frequency with about 80 Hz mainly occurs in the periods of, for example,  $t = 0.45 \sim 0.5$  s and  $0.8 \sim 0.9$  s, while for  $L/D = 4.0$ , a dominant frequency with about 60 Hz occurs in the period of  $t = 0.5 \sim 0.9$  s. This observation indicates that the motion of the film during these stages possesses clear periodicity. Conversely, for regions that do not include transient dominant frequency in the time-frequency spectra, the corresponding film motion features aperiodicity. Besides, the amplitude of the trailing edge in the periodic stages is larger than that in the irregular stage, as demonstrated by the time histories in region (i) and region (ii) of Figs. 3(a) and 4(a). Despite the occurrence of the transient periodic stages in the time-frequency spectra, it is noteworthy that the motion of the film is still irregular in terms of the overall view.

According to the CWT spectra, we can extract the deformation sequences of the film in the periodic stage and the aperiodic stage, respectively, as shown in Figs. 3(c) and 3(d) for  $L/D = 3.0$  and Figs. 4(c) and 4(d) for  $L/D = 4.0$ . During the periodic stage, the film's deformation is primarily characterized by the flection mode; correspondingly, the envelope of the film deformation exhibits a visible convergence. In Figs. 3 and 4, the convergent points are located at  $x/D = 2.43$  ( $s/L = 0.81$ ) for  $L/D = 3.0$ , and at  $x/D = 3.15$  ( $s/L = 0.79$ ) for  $L/D = 4.0$ . It is pertinent to mention that the

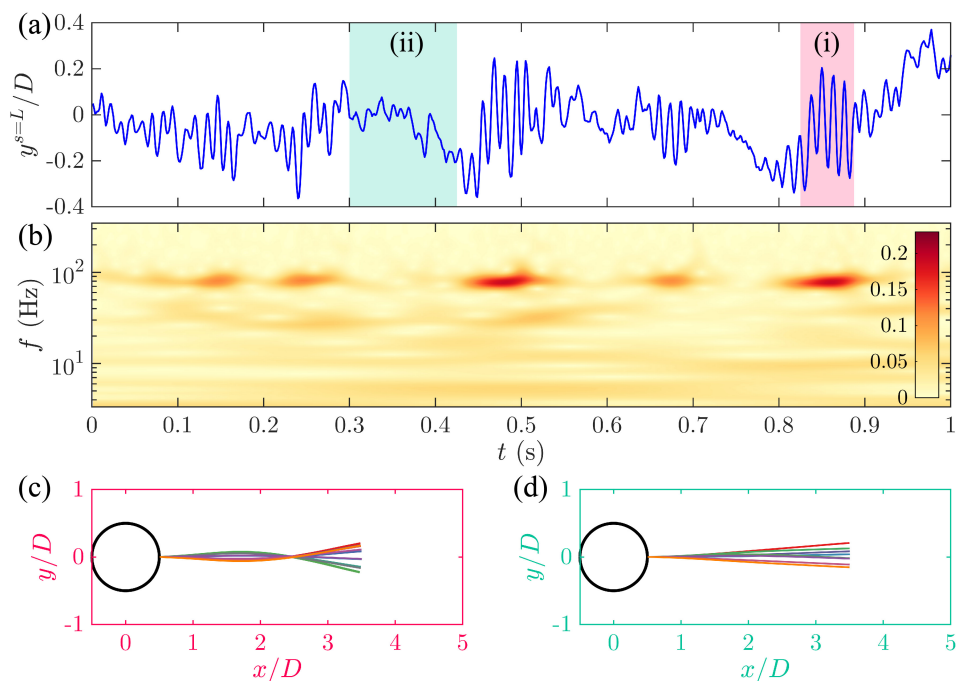


**Figure 3.** Hybrid flutter in the case of  $L/D = 3.0$ . (a) Time history of the  $y$ -directional displacement of the trailing edge within 1 second. (b) Continuous wavelet transform of the data in panel (a). (c) Flection mode of the hybrid flutter, corresponding to the time trace in the light red region (i) of panel (a). (d) Deflection mode of the hybrid flutter, corresponding to the time trace in the light green region (ii) of panel (a).

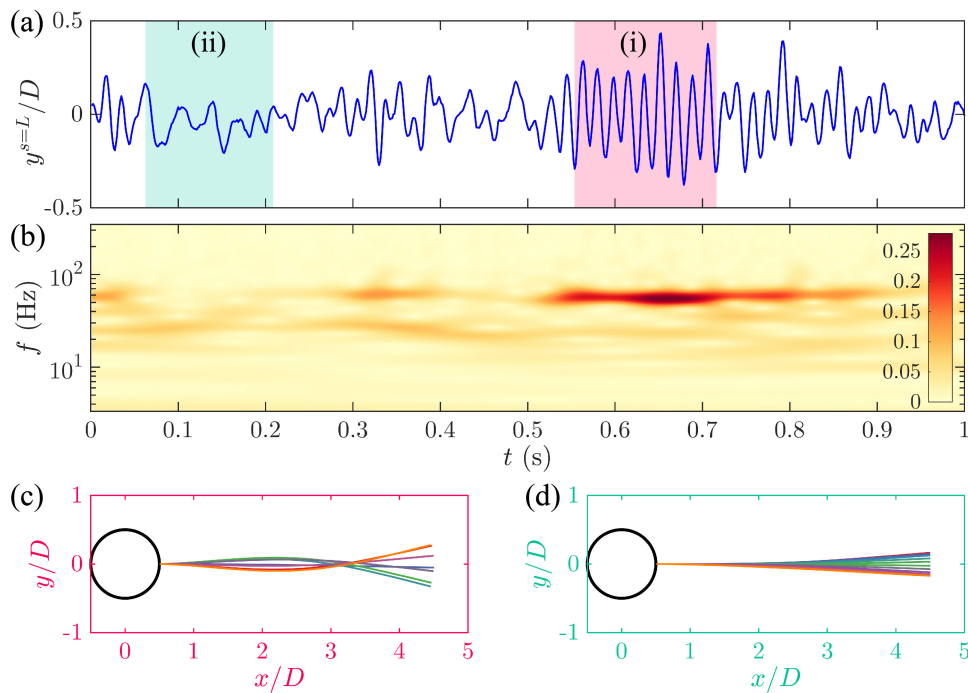


**Figure 4.** Hybrid flutter in the case of  $L/D = 4.0$ . The captions for panels (a) to (d) here are the same as those in Fig. 3 in a one-by-one manner.

location of the convergent points at different periodic stages may fluctuate in the small region near  $s/L = 0.8$ . These results accord well with the features of the second-order intrinsic mode of a cantilever beam, which has a node at about  $s/L = 0.8$  (Dutta et al., 2011). In the aperiodic stages, the film only deforms with the deflection mode (the first-order mode), and the corresponding envelope tends to a linear increase from the leading edge to the trailing edge.

Based on the synchronized measurement of the flow fields and the film deformations, we can further explore how the flow structures evolve as the film motion is characterized by different modes. Here, the virtual dye visualization technique is employed to track the Lagrangian coherent structures (LCS) in the flow field (He et al., 2017). Dye visualization (including hydrogen bubbles, smoking lines, fluorescent particles, etc.) is a common tool in experimental fluid mechanics, which is powerful in revealing the flow structures in fluid flow. Plenty of classical phenomena in fluid mechanics are revealed by dye visualization for the first time, such as the boundary layer transition and the vortex shedding. In comparison to the traditional dye visualization using real particles, the virtual dye visualization based on the measured velocity fields from PIV has several advantages. The virtual particles can be seeded anywhere in the flow field. The particle density can be precisely controlled. By assigning different colors to the virtual particles at different releasing locations, the complex interactions between different coherent structures can be clearly revealed (He et al., 2017). Moreover, the trackability of the release time for each virtual particle enables the analysis of the evolving history of specific flow structures. This capability presents a unique advantage not found in alternative methods for detecting Lagrangian coherent structures (LCSs), such as finite-time Lyapunov exponents (Green et al., 2007). In Figs. 5 to 8, virtual tracers are released simultaneously from the upper and the lower shear layer to the flow fields; then, these tracers convect with the flow based on the measured velocity fields using the “pseudo-tracing” algorithm (Jensen et al., 2003). The evolution of the tracers, therefore, reveals the flow structures in the flow fields.

Figures 5 and 6 present the evolution of LCSs during the film deforming with the deflection mode. The formation, shedding, and convection of the large-scale vortices are revealed clearly by the virtual dye visualization. To clarify the interactions between different vortices, we prescribe blue and red colors for the tracers released from the upper and lower shear layers, respectively. For both the cases of  $L/D = 3.0$  and  $L/D = 4.0$ , the vortices are alternately formed against the film’s surfaces and evolve in the form of a standard periodic Kármán vortex street. The large-scale vortices are attracting structures in the flow field (Alben, 2012). Thus, the periodic vortices evolving on both sides of the film exert forces with opposite orientations on the different positions of the film, which is the reason for the film’s periodic deflection. In this periodic stage, a mutual lock-in between the motion of the film and the evolution of the vortices emerges due to the same dominant frequencies between them. Compared with  $L/D = 3.0$ , the formation length and the wavelength of the periodic vortices show a substantial increase in the case of  $L/D = 4.0$ . The vortex formation lengths for  $L/D = 3.0$  and  $L/D = 4.0$  are about  $2.7D$  and  $3.2D$ , respectively, which can be determined by conditional statistics of the streamwise velocity fields (refer to Duan & Wang (2024)). The wave-

lengths of vortices for the two cases estimated from the LCSs in Figs. 5 and 6 are approximately  $4.5D$  and  $6.6D$ , respectively. Besides, the vortices in the case of  $L/D = 4.0$  appear to be stretched, which can be ascribed to the larger formation length in this case (Figs. 6b to 6d).

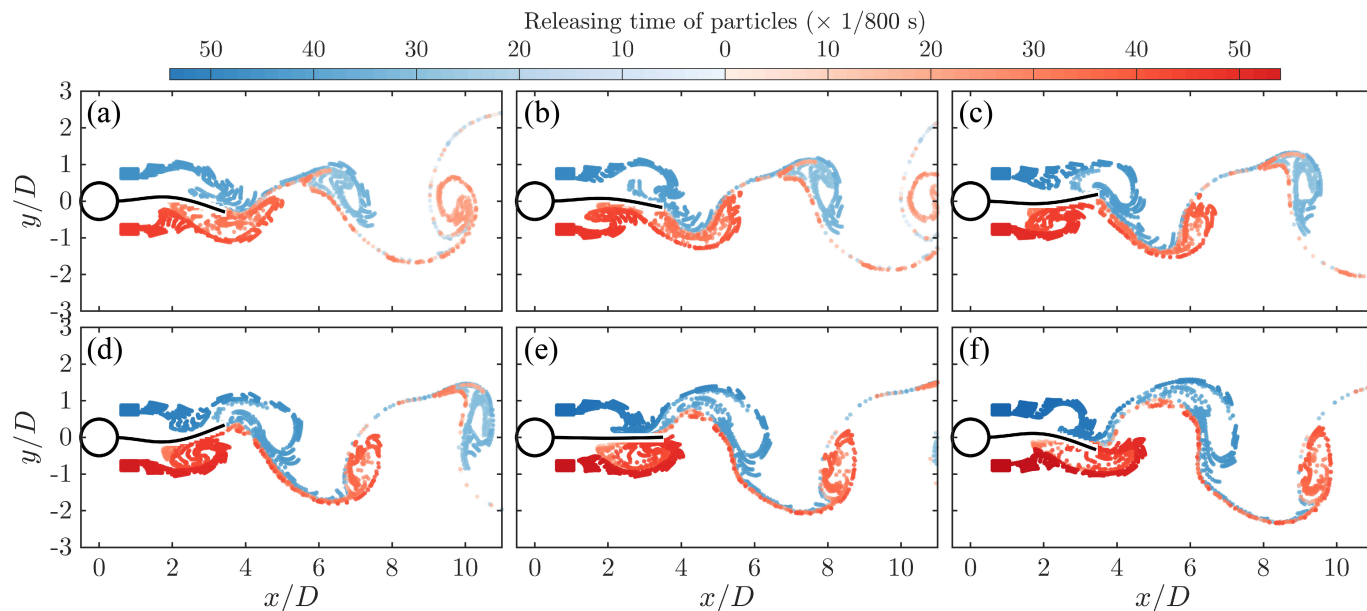


**Figure 5.** Lagrangian coherent structures obtained by virtual dye visualization during the flecnion mode of the  $L/D = 3.0$  film. (a-f) Six successive frames of the flow fields with a time interval between adjacent panels of  $3/800$  s. The blue particles are released from the upper shear layer while the red particles from the lower shear layer. The color gradients indicate when the particles are released into the flow fields.

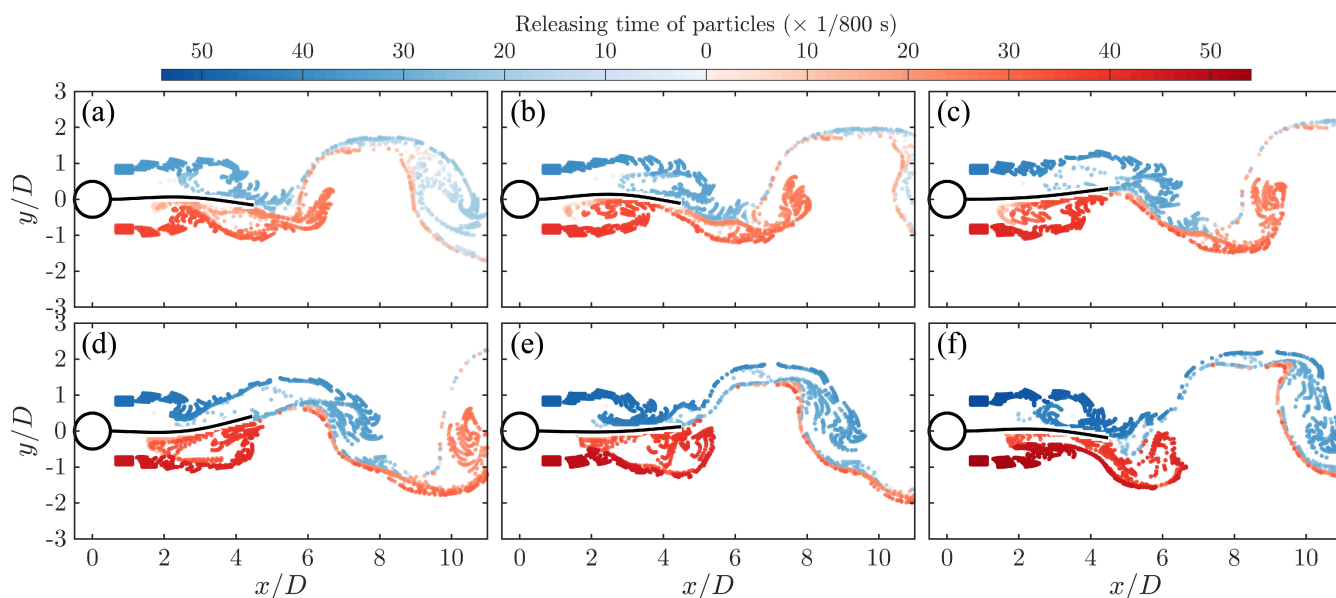


**Figure 6.** Caption for this figure are the same as that for Fig. 5. The film length here is  $L/D = 4.0$ .

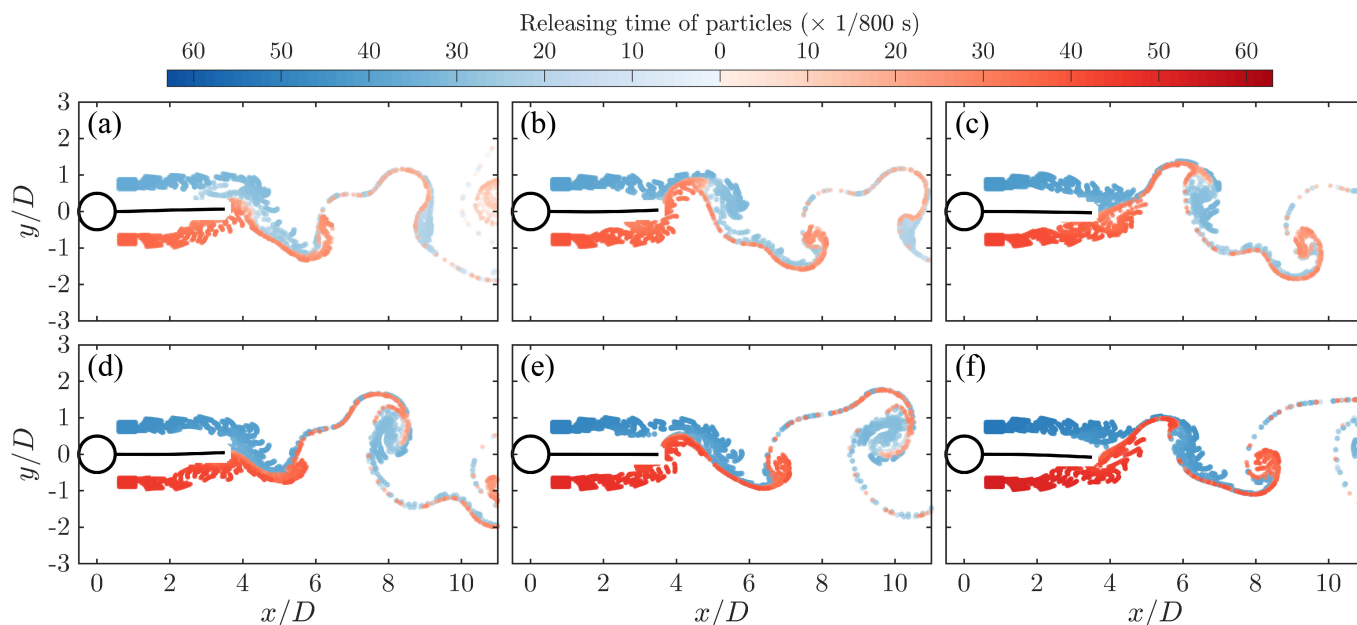


**Figure 7.** Lagrangian coherent structures obtained by virtual dye visualization during the deflection mode of the  $L/D = 3.0$  film. (a-f) Six successive frames of the flow fields with a time interval between adjacent panels of  $3/800$  s. The meaning of colors gradients here is the same as that in Fig. 5.

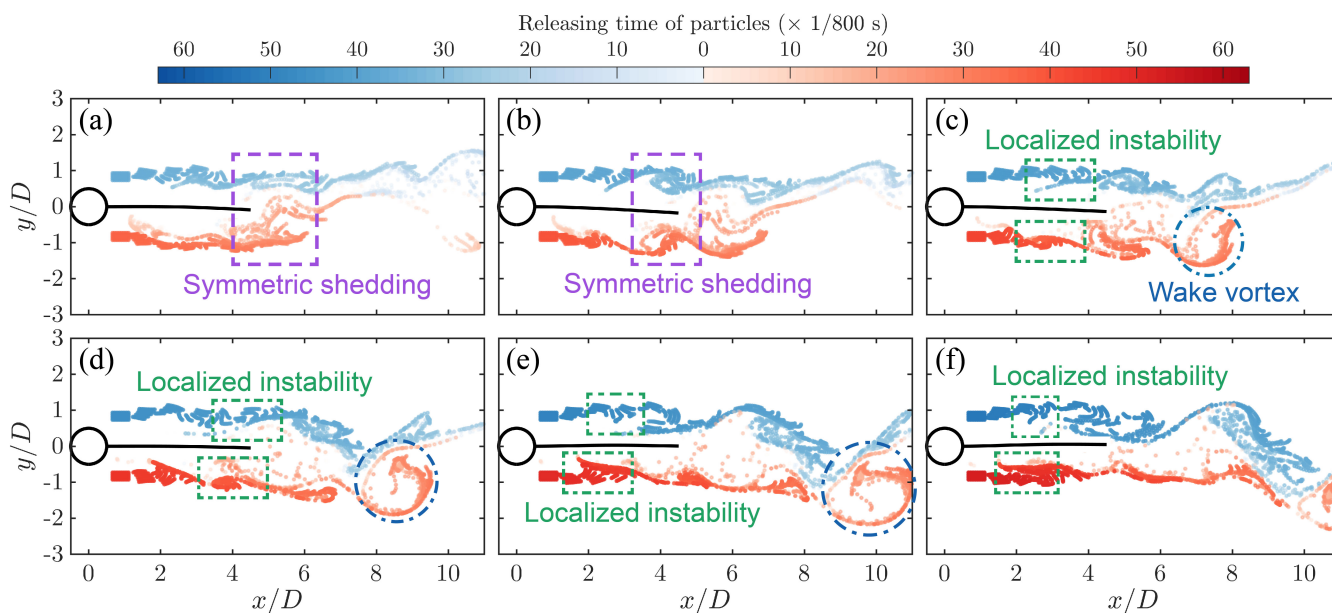


**Figure 8.** Lagrangian coherent structures obtained by virtual dye visualization during the deflection mode of the  $L/D = 4.0$  film. Captions for panels (a-f) here have one-by-one correspondences to those in Fig. 7. The purple dashed boxes highlight the symmetric shedding of the vortices; the green dash-dotted boxes highlight the localized instabilities of the separated shear layers; the blue dash-dotted circles highlight the large-scale vortex formed in the downstream wake.

After transitioning to the aperiodic deflection mode, the interactions become more complicated and the flow structures also tend to be disordered. As presented in Figs. 7 and 8, the LCSs are not as regular as those during the flection mode of the film (Figs. 5 and 6). For  $L/D = 3.0$ , the separated shear layers extend downstream along the film and culminate in the formation of the large-scale vortices downstream the trailing edge of the film, rather than on the surfaces of the film. This process is distinctly illustrated in Figs. 7(b) to 7(d). Subsequent to being shed into the wake, these vortices sometimes undergo significant stretching, rendering the wake challenging to sustain a regular Kármán vortex street; as shown in Figs. 7(a) to 7(c), the anti-clockwise vortex is stretched into a vortex thread without a distinct recirculation shape. Also, some vortices can maintain the typical recirculation structure, for example, the clockwise vortex in Figs. 7(b) to 7(d). Notwithstanding the stretching of the vortices, the wake for  $L/D = 3.0$  can still keep an oscillatory characteristic (Fig. 7). However, in the case of  $L/D = 4.0$ , the oscillatory characteristic of the wake even disappears. As shown in Figs. 8, the shear layers on both sides of the film experience an approximately symmetric evolution accompanied by the final symmetric vortex shedding (Fig. 8a and 8b), resulting in the wake like a turbulent jet. If the symmetric vortices have a significant strength difference, there will be competition between them in the wake. The stronger one will dominate the wake, evolving into a large-scale vortex in the downstream wake, as shown by the wake vortex in Figs. 8(c) to 8(e). During the persistent extension of the shear layers along the film, they exhibit localized instabilities, as highlighted by the green boxes in Figs. 8(c) to 8(f). As the approximately symmetric localized instabilities of the upper and the lower shear layers reach the trailing edge of the film, they finally bring about the symmetric vortex shedding (Figs. 8c and 8d). In comparison, for  $L/D = 3.0$ , the shear layers show no localized instability as they extend along the film; instead, the separated shear layers steadily develop until the large-scale vortices are formed downstream of the trailing edge (Fig. 7). Although the development of the separated shear layers and the evolution of vortex structures between deflection modes of  $L/D = 3.0$  and  $L/D = 4.0$  have perceptible differences, the films are always enveloped by the elongated shear layers in these two cases, lacking periodic alternating forces exerted on the film. As a result, the aperiodic deflection flutter of the film arises.

#### 4. Conclusions

In this experimental investigation, the stress is paid to the hybrid flutter of the film at certain lengths,  $L/D = 3.0$  and  $L/D = 4.0$ . The flow fields and the film deformations are measured synchronously with a two-dimensional time-resolved PIV system. The analyses for the transient deformation modes and the flow structure evolution are performed to explore the fluid-structure interaction mechanisms underlying different motion modes during the hybrid flutter. It is determined that this hybrid flutter is irregular in terms of the overall view, where the film intermittently exhibits second-order flection mode and first-order deflection mode. With the aid of the

continuous wavelet transform, it is found that when the film adopts the flection mode, there is a significantly dominant frequency, whereas the dominant frequency disappears in the CWT spectrum upon the film flutter transitioning to the deflection mode. Based on the Lagrangian coherent structures revealed by virtual dye visualization, it is identified that the periodic flection of the film is attributed to the coupling process whereby the large-scale vortices are alternately formed on the film and, therefore, act periodic alternating forces on the film's surfaces. After the large-scale vortices being released into the wake, they evolve in the form of a Kármán vortex street. Hence, during the flection mode, both the film motion and the flow field evolution possess a periodic nature.

In comparison, as the film deforms with the deflection mode, the coupling mechanisms are more complicated. For  $L/D = 3.0$ , the large-scale vortices are no longer formed on the film, instead, downstream of the film's trailing edge; hence, the whole film is enveloped by the elongated shear layers separated from the cylinder. Furthermore, stretching of vortices occurs in the wake, which leads to a degree of the irregularity of the wake. In the case of  $L/D = 4.0$ , the shear layers exhibit approximately symmetric extension along the film, during which there is localized instability in the shear layers but without the formation of large-scale vortices. The occurrence of localized instability means the length of  $L/D = 4.0$  exceeds the length limit that the shear layers can undergo steady extension. During the deflection mode, irrespective of  $L/D = 3.0$  and  $4.0$ , the film is always enveloped by the elongated shear layers, so that no periodic alternating force is yielded on the film surfaces as it interacts with ambient flow fields; consequently, the film undergoes aperiodic flutter with the first-order mode. Based on the above results, it is evident that "hybrid flutter" means not only the transition of film's motion modes, but also the associated intermittent alternation of periodic and aperiodic processes within the coupling system.

## Acknowledgements

The authors would like to acknowledge the support for this work from National Science Foundation of China (Grant Number: 12127802).

## Nomenclature

$b$	Spanwise length [m]
$B$	Bending stiffness [ $\text{N m}^2$ ]
$D$	Cylinder diameter [mm]
$E$	Young's modulus [MPa]
$h$	Thickness of the film [mm]
$K_B$	Effective bending stiffness

$L$	Streamwise length of the film [mm]
$S$	Mass ratio
$t$	Time coordinate [s]
$x$	Streamwise Cartesian coordinate [mm]
$y$	Vertical Cartesian coordinate [mm]
$z$	Spanwise Cartesian coordinate [mm]
$\rho_f$	Density of the oncoming flow [ $\text{kg m}^{-3}$ ]
$\rho_s$	Density of the film [ $\text{kg m}^{-3}$ ]

## References

- Alben, S. (2012, April). The attraction between a flexible filament and a point vortex. *Journal of Fluid Mechanics*, 697, 481–503. doi: 10.1017/jfm.2012.78
- Champagnat, F., Plyer, A., Le Besnerais, G., Leclaire, B., Davoust, S., & Le Sant, Y. (2011, April). Fast and accurate PIV computation using highly parallel iterative correlation maximization. *Experiments in Fluids*, 50(4), 1169–1182. doi: 10.1007/s00348-011-1054-x
- Cui, G.-P., Feng, L.-H., & Hu, Y.-W. (2022, April). Flow-induced vibration control of a circular cylinder by using flexible and rigid splitter plates. *Ocean Engineering*, 249, 110939. doi: 10.1016/j.oceaneng.2022.110939
- Duan, F., & Wang, J. (2021, August). Fluid–structure–sound interaction in noise reduction of a circular cylinder with flexible splitter plate. *Journal of Fluid Mechanics*, 920, A6. doi: 10.1017/jfm.2021.403
- Duan, F., & Wang, J.-J. (2024, May). Passive bionic motion of a flexible film in the wake of a circular cylinder: Chaos and periodicity, flow–structure interactions and energy evolution. *Journal of Fluid Mechanics*, 986, A29. doi: 10.1017/jfm.2024.327
- Dutta, R., Ganguli, R., & Mani, V. (2011, October). Swarm intelligence algorithms for integrated optimization of piezoelectric actuator and sensor placement and feedback gains. *Smart Materials and Structures*, 20(10), 105018. doi: 10.1088/0964-1726/20/10/105018
- Furquan, M., & Mittal, S. (2021, June). Multiple lock-ins in vortex-induced vibration of a filament. *Journal of Fluid Mechanics*, 916, R1. doi: 10.1017/jfm.2021.209
- Gonzalez, R., & Woods, R. (2017). *Digital Image Processing* (4th edition ed.). New York, NY: Pearson.

- Green, M. A., Rowley, C. W., & Haller, G. (2007, February). Detection of Lagrangian coherent structures in three-dimensional turbulence. *Journal of Fluid Mechanics*, 572, 111–120. doi: 10.1017/S0022112006003648
- He, G.-S., Wang, J.-J., Pan, C., Feng, L.-H., Gao, Q., & Rinoshika, A. (2017, February). Vortex dynamics for flow over a circular cylinder in proximity to a wall. *Journal of Fluid Mechanics*, 812, 698–720. doi: 10.1017/jfm.2016.812
- Jensen, A., Pedersen, G. K., & Wood, D. J. (2003, June). An experimental study of wave run-up at a steep beach. *Journal of Fluid Mechanics*, 486, 161–188. doi: 10.1017/S0022112003004543
- Lee, J., & You, D. (2013, November). Study of vortex-shedding-induced vibration of a flexible splitter plate behind a cylinder. *Physics of Fluids*, 25(11), 110811. doi: 10.1063/1.4819346
- Liao, J. C. (2007, November). A review of fish swimming mechanics and behaviour in altered flows. *Philosophical Transactions of the Royal Society B: Biological Sciences*, 362(1487), 1973–1993. doi: 10.1098/rstb.2007.2082
- Mallat, S. (1999). *A Wavelet Tour of Signal Processing* (Second Edition ed.). USA: Elsevier.
- Miles, J. G., & Battista, N. A. (2019, September). Naut Your Everyday Jellyfish Model: Exploring How Tentacles and Oral Arms Impact Locomotion. *Fluids*, 4(3), 169. doi: 10.3390/fluids4030169
- Pfister, J.-L., & Marquet, O. (2020, August). Fluid–structure stability analyses and nonlinear dynamics of flexible splitter plates interacting with a circular cylinder flow. *Journal of Fluid Mechanics*, 896, A24. doi: 10.1017/jfm.2020.284
- Sahu, T. R., Furquan, M., & Mittal, S. (2019, December). Numerical study of flow-induced vibration of a circular cylinder with attached flexible splitter plate at low. *Journal of Fluid Mechanics*, 880, 551–593. doi: 10.1017/jfm.2019.699
- Sharma, K. R., & Dutta, S. (2020, January). Flow control over a square cylinder using attached rigid and flexible splitter plate at intermediate flow regime. *Physics of Fluids*, 32(1), 014104. doi: 10.1063/1.5127905
- Shelley, M., Vandenberghe, N., & Zhang, J. (2005, March). Heavy Flags Undergo Spontaneous Oscillations in Flowing Water. *Physical Review Letters*, 94(9), 094302. doi: 10.1103/PhysRevLett.94.094302
- Shelley, M. J., & Zhang, J. (2011, January). Flapping and Bending Bodies Interacting with Fluid Flows. *Annual Review of Fluid Mechanics*, 43(1), 449–465. doi: 10.1146/annurev-fluid-121108-145456

- Shukla, S., Govardhan, R., & Arakeri, J. (2023, October). Flow over a circular cylinder with a flexible splitter plate. *Journal of Fluid Mechanics*, 973, A19. doi: 10.1017/jfm.2023.755
- Taguchi, M., & Liao, J. C. (2011, May). Rainbow trout consume less oxygen in turbulence: The energetics of swimming behaviors at different speeds. *Journal of Experimental Biology*, 214(9), 1428–1436. doi: 10.1242/jeb.052027
- Taylor, G., Burns, J., Kammann, S., Powers, W., & Welsh, T. (2001). The Energy Harvesting Eel: A small subsurface ocean/river power generator. *IEEE Journal of Oceanic Engineering*, 26(4), 539–547. doi: 10.1109/48.972090
- Wang, J.-S., & Wang, J.-J. (2021, July). Vortex dynamics for flow around the slat cove at low Reynolds numbers. *Journal of Fluid Mechanics*, 919, A27. doi: 10.1017/jfm.2021.385
- Wang, T., Ren, Z., Hu, W., Li, M., & Sitti, M. (2021, May). Effect of body stiffness distribution on larval fish-like efficient undulatory swimming. *Science Advances*, 7(19), eabf7364. doi: 10.1126/sciadv.abf7364
- Webb, P.W. (1998, August). Entrainment by river chub *Micropterus dolomieu* and smallmouth bass *Micropterus dolomieu* on cylinders. *Journal of Experimental Biology*, 201(16), 2403–2412. doi: 10.1242/jeb.201.16.2403
- Yu, Y., & Liu, Y. (2015, May). Flapping dynamics of a piezoelectric membrane behind a circular cylinder. *Journal of Fluids and Structures*, 55, 347–363. doi: 10.1016/j.jfluidstructs.2015.03.009